

DYNAMICAL ANALYSIS OF A PARAMETRICALLY FORCED MAGNETO-MECHANICAL OSCILLATOR

JULIAN STRATEMEIER ¹, COURTNEY QUINN ¹ and LAWRENCE K. FORBES ¹

(Received 19 June, 2024; accepted 7 January, 2025)

Abstract

This study explores the dynamics of a simple mechanical oscillator involving a magnet on a spring constrained to an axis; this magnet is additionally subject to the attractive force from a second magnet, which is placed on a parallel offset axis. The moments of both magnets remain aligned. The dynamics of the first magnet is first analysed in isolation for an unforced situation in which the second magnet is static and its position is taken as a parameter. We find codimension-1 saddle-node bifurcations, as well as a codimension-2 cusp bifurcation. The system has a region of bistability which increases in size with increasing force ratio. Next, the parametrically forced situation is considered, in which the second magnet moves sinusoidally. A comprehensive analysis of the forced oscillator behaviour is presented from the dynamical-systems standpoint. The solutions are shown to include periodic, quasiperiodic and chaotic trajectories. Resonances are shown to exist and the effect of weak damping is explored. Layered stroboscopic maps are used to produce cross-sections of the chaotic attractor as the parametric forcing frequency is varied. The strange attractor is found to disappear for a narrow window of forcing frequencies near the natural frequency of the spring.

1. Introduction

Spring–mass systems in classical mechanics represent a rich source of linear and nonlinear differential and difference equations, and the amount of literature on such devices is vast. Nonlinear effects typically arise in these systems in one of two forms. One possibility is related to *material* nonlinearity, in which the substance from which the device is made does not follow a simple, linear Hooke’s law relation between the material response and an applied force, but instead acts either as a hardening or softening spring. Possibly the most famous example of such behaviour is observed in the Duffing equation, described in texts such as that by Guckenheimer and Holmes

¹School of Natural Sciences, University of Tasmania, Hobart, Tasmania 7005, Australia;
e-mail: julians5@utas.edu.au, courtney.quinn@utas.edu.au, larry.forbes@utas.edu.au

© The Author(s), 2025. Published by Cambridge University Press on behalf of Australian Mathematical Publishing Association Inc. This is an Open Access article, distributed under the terms of the Creative Commons Attribution licence (<https://creativecommons.org/licenses/by/4.0>), which permits unrestricted re-use, distribution and reproduction, provided the original article is properly cited.

[5, Section 2.2]. Alternatively, *geometrical nonlinearity* exists in systems where the springs follow Hooke's law with a linear force-displacement relationship, but they are not aligned with the direction of motion and so are always acting at some location-dependent angle to it. A particularly simple example of this is given by Forbes [4] and, more recently, Pal et al. [14] studied the role of pure geometric nonlinearity in modelling continua using a lattice of masses connected by linear springs.

Additional applications for the dynamics of nonlinear mechanical oscillators include devices used for vibration isolation [7], vibration absorption [8] and energy harvesting [17]. Magneto-mechanical oscillators involving magnetic and elastic forces are popular choices for study, and were also some of the first systems to be used by Moon and Holmes [12] to investigate chaotic motions in structural mechanics. More recent papers performed dynamical analyses of oscillators consisting of permanent magnets attached to elastic beams and demonstrated good agreement with experiments. Some instances of such work are given by Kumar et al. [10] and Hao et al. [6]. Sarafian [15] successfully modelled the dynamics of two repelling permanent magnets, dropped into a vertical tube, as a dipole-dipole interaction. For aligned dipoles, the magnetic force drops off as the inverse fourth power of the dipole separation [18], resulting in highly nonlinear dynamics. The recent review article by Yan et al. [16] shows many different electro-mechanical devices used in vibration isolation and discusses some of their nonlinear responses near resonance.

An intriguing modern application of these studies is to “energy harvesting” devices. The idea is that many current monitoring devices are so reduced in size that they only require very small amounts of energy to continue to function. They accumulate these energy inputs by taking advantage of the (otherwise undesirable) vibrations of the environment in which they are situated. A recent review of these types of devices is given by Chen and Fan [1], and discusses their use in medical and health monitoring. Mann and Owens [11] studied a nonlinear energy harvester device that used a combination of oscillating and fixed magnets to produce a bi-stable potential well, and their experimental results confirmed that nonlinearity can make such a device more robust by increasing its frequency response.

In this present paper, we similarly use a dipole-dipole interaction to model magnetic forces between magnets, but here, we also include some naturally occurring effects of geometric nonlinearity. We provide a dynamical analysis of a simple yet novel one-degree-of-freedom nonlinear magneto-mechanical oscillator. The system consists of two permanent magnets (modelled as aligned point dipoles) confined to move on parallel offset axes. We are concerned with the motion of magnet 1 under the combined effects of a linear spring restoring force and an attracting magnetic force from magnet 2. When the position of this second magnet is oscillated periodically in time, our oscillator then becomes a Hamiltonian system subjected to a parametric excitation; these systems often display interesting dynamics, such as chaotic solutions arising from perturbed homoclinic connections or the appearance of resonant tori [5].

This paper is structured as follows. In Section 2, we outline the model and physical assumptions, and derive the dimensionless governing equation (2.2) on which our

analysis and numerical solutions are based. This is a nonlinear, parametrically forced second-order differential equation. Section 3 first focusses on the undamped and unforced case. We present a somewhat novel parametrization method that allows us to track the behaviour of equilibria as our two key dimensionless parameters are varied and produce the appropriate bifurcation diagrams. In addition, it allows us to calculate the location of the key codimension-2 bifurcation point in closed form in the parameter plane. Periodic forcing of the location of magnet 2 is then considered in Section 5. The governing equation (2.2) for the position of magnet 1 then gives rise to a parametrically forced nonlinear system. Possible solution behaviour types are identified and characterized using phase plane plots, time series, power spectra, strobe maps and Lyapunov exponents. The effect of weak damping on solution behaviour is briefly illustrated and layered stroboscope maps are used to investigate some consequences of varying the frequency of the periodic forcing of magnet 2. A summary and discussion is presented in Section 6.

2. The magneto-mechanical oscillator system

The mechanical device of interest here is sketched in Figure 1. It consists of two permanent magnets, each of which is attached to a bead that slides without friction along its own smooth fixed rod. The two rods are parallel and are separated by distance h . As indicated in Figure 1, magnet 1 is attached to a rigid wall by a classical Hookean spring and its displacement $x_1(t)$ along its rod is measured from the end of the unstretched spring, at which the origin O on the x -axis is located. The spring constant is $k_1 \text{ N m}^{-1}$ and so magnet 1 experiences a Hookean restoring force $F_s = -k_1 x_1$. Magnet 2 acts on magnet 1 via a magnetic force F . To simplify analysis, we model both magnets as perfect (point) dipoles with positions x_1 and x_2 , which will be a good approximation when the separation r between magnets is large compared with magnet dimensions. We further assume the magnetic dipole moments \mathbf{m}_1 and \mathbf{m}_2 remain aligned as the magnets move along the rod in an attracting configuration; thus, the magnets will be free to rotate on their beads and thus change their angle continuously as they move. Note that the dependent variables of interest in this model are the position $x_1(t)$ and velocity $v_1(t)$ of magnet 1. By contrast, the position $x_2(t)$ of magnet 2 is known in advance, since that magnet is either stationary or else is forced to move sinusoidally by an external driving mechanism such as a piston, for example. Thus, x_2 is considered to be a parameter and the effects of sinusoidally varying this parameter with time is explored in Section 5.

We now analyse the forces on magnet 1 and thus derive its equation of motion. Because the spring is taken to be Hookean and at natural extension when $x_1 = 0$, it is subject to a restoring force $F_s = -kx_1$. In addition, the magnetic force on magnet 1 from the field of magnet 2 given by Yung et al. [18] is

$$F = \frac{M}{r^4},$$

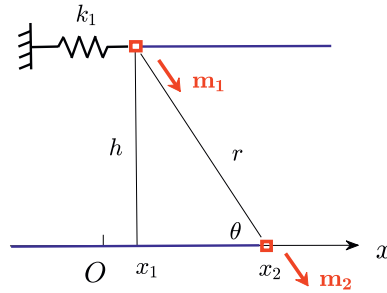


FIGURE 1. Schematic of the magneto-mechanical oscillator system. The magnets are attached to beads (red squares) which slide freely along the rods (blue lines). Magnet 1 and magnet 2 have positions $x_1(t)$ and $x_2(t)$, respectively. The parameters are as follows: \mathbf{m}_1 and \mathbf{m}_2 are the associated magnetic dipole moments, k_1 is the spring constant, r is the separation between the magnets, θ is the acute angle of the dipole moment relative to the x -axis and h is the distance between the fixed rods. We consider the x -component of the magnetic force F_x acting on the top magnet.

in which r is the separation between the magnets, as depicted in Figure 1. The constant $M = (3\mu_0|\mathbf{m}_1||\mathbf{m}_2|)/(2\pi) \text{ N m}^4$ gives a measure of the overall “strength” of the magnets. Here, μ_0 is the magnetic permeability of free space. From Figure 1, the separation between the magnets is $r = \sqrt{h^2 + (x_2 - x_1)^2}$ and θ is the angle of the dipole moments relative to the x -axis. Consequently, the x -component of the magnetic force F is

$$F_x = F \cos \theta = \left(\frac{M}{r^4}\right)\left(\frac{x_2 - x_1}{r}\right) = \frac{M(x_2 - x_1)}{[h^2 + (x_2 - x_1)^2]^{5/2}}.$$

Finally, we also assume that magnet 1 experiences a linear damping force proportional to its velocity. These forces are now combined into Newton’s second law, using d_1 (Ns m^{-1}) as the damping coefficient and m_1 (kg) as the mass of magnet 1. This yields an equation of motion for magnet 1, which takes the form

$$m_1 \frac{d^2x_1}{dt^2} = F_s + F_x - d_1 \frac{dx_1}{dt} = -k_1x_1 + \frac{M(x_2 - x_1)}{[h^2 + (x_2 - x_1)^2]^{5/2}} - d_1 \frac{dx_1}{dt}. \quad (2.1)$$

It is convenient now to express the governing equation (2.1) in dimensionless form. We define a nondimensional time $\tau = t/t_c$ and a dimensionless position of mass 1 to be $\chi(\tau) = x_1(t)/x_c$, in which the time scale t_c (s) and length scale x_c (m) are free to be chosen. These new variables are introduced into the equation of motion (2.1) and here, we choose the time scale and length scale to be

$$t_c = \sqrt{\frac{m_1}{k_1}}; \quad x_c = \frac{M}{k_1 h^4}.$$

After a little algebra, the dimensionless equation of motion corresponding to (2.1) is found to be

$$\frac{d^2\chi}{d\tau^2} + D \frac{d\chi}{d\tau} + \chi - \frac{A - H\chi}{[1 + (A - H\chi)^2]^{5/2}} = 0. \quad (2.2)$$

We define the three dimensionless parameters:

$$H = \frac{x_c}{h} = \frac{M}{k_1 h^5}; \quad D = \frac{d_1}{\sqrt{k_1 m_1}}; \quad A = \frac{x_2}{h}. \quad (2.3)$$

The constant H is simply the inverse of the separation distance h between the two rods in Figure 1 made dimensionless with respect to the length scale x_c . However, from the first definition in (2.3), constant H can also be regarded as a measure of the ratio of the magnetic force to the spring force. The second quantity D in (2.3) is the nondimensionalized damping coefficient and parameter A is the dimensionless location of magnet 2 relative to the origin O in Figure 1.

If the location of magnet 2 is held fixed, then the parameter A in (2.3) is just some constant A_0 that is specified in advance. However, the location of magnet 2 will also be considered to be forced periodically. The corresponding dimensionless form for the position of magnet 2 is

$$A \equiv A(\tau) = A_0 + \epsilon \cos(\Omega\tau). \quad (2.4)$$

Here, we define the three constants:

$$A_0 = \frac{A_1 + A_2}{2}; \quad \epsilon = \frac{A_2 - A_1}{2}; \quad \Omega = \omega t_c. \quad (2.5)$$

The mean location of magnet 2 in dimensionless form is A_0 and its forcing amplitude is ϵ . The two constants A_1 and A_2 are the nondimensional bounds of the periodic variation in the position of magnet 2 along the x -axis. The final constant Ω in (2.5) is the nondimensional forcing frequency.

We re-cast the second-order equation (2.2) as an equivalent system of two first-order equations by defining the dimensionless velocity $v = d\chi/d\tau$ in the obvious manner. The final form of the governing equations is thus

$$\begin{aligned} \frac{d\chi}{d\tau} &= v, \\ \frac{dv}{d\tau} &= \frac{A - H\chi}{[1 + (A - H\chi)^2]^{5/2}} - \chi - Dv. \end{aligned} \quad (2.6)$$

This system models the simple mechanical device depicted in Figure 1. It bears some similarity to the magnetic pendulum, in which a permanent magnet is attached to the bob at the end of a pendulum hanging down under the effects of gravity. The pendulum is free to move in any direction across the face of a horizontal (x, y) plane. A few magnets are fixed at various points on the plane and the pendulum is set in motion. Depending on its initial position and velocity, the pendulum can trace out

paths of enormous complexity, and a recent introductory description of such a device is given by Christian and Middleton-Spencer [2]. Our system in Figure 1 is superficially simpler than a magnetic pendulum, in the sense that it is constrained to move in one spatial direction only; nevertheless, it is no longer an autonomous, integrable system when it is forced by the periodic motion (2.4) of magnet 2, and so it, too, is capable of motion of enormous complexity.

3. Undamped and unforced case

This section considers the situation in which damping is ignored ($D = 0$) and the system is not forced, so that magnet 2 has the fixed location $A = A_0$. In this case, the equations of motion (2.6) are autonomous and become

$$\begin{aligned} \frac{d\chi}{d\tau} &= v, \\ \frac{dv}{d\tau} &= \frac{A_0 - H\chi}{[1 + (A_0 - H\chi)^2]^{5/2}} - \chi. \end{aligned} \quad (3.1)$$

3.1. Equilibria and bifurcations in A We solve for equilibria $(\chi_{\text{eq}}, v_{\text{eq}})$ by setting the derivatives in the system (3.1) to zero. This immediately gives $v_{\text{eq}} = 0$ as expected on physical grounds, but the equation for χ_{eq} must be solved numerically. For illustrative purposes, in the following analysis, we show some results for $H = 10$, as this is a reasonable value for a physical oscillator one could construct from permanent magnets¹. (The effect of varying both H and A_0 is discussed later in Section 3.2.) At $A_0 = 0$, we obtain an equilibrium value $\chi_{\text{eq}} \approx 0.0248$ using Newton's method.

We then construct a bifurcation diagram that tracks χ_{eq} as A_0 is increased from zero. The bifurcation diagram is generated exactly by employing a parametrization approach, which we briefly outline here. For a fixed value of H , we solve

$$\chi_{\text{eq}} = \frac{A_0 - H\chi_{\text{eq}}}{[1 + (A_0 - H\chi_{\text{eq}})^2]^{5/2}}. \quad (3.2)$$

We seek χ_{eq} and A_0 as functions of a parameter θ . Thus, the change of variable $H\chi_{\text{eq}} = A_0 - \tan \theta_{\text{eq}}$ is made in (3.2). This gives rise to the algorithm:

- give values of the parameter θ_{eq} : $0 < \theta_{\text{eq}} < \pi/2$;
- calculate $\chi_{\text{eq}} = \sin \theta_{\text{eq}} \cos^4 \theta_{\text{eq}}$ from (3.2);
- create $A_0 = \tan \theta_{\text{eq}} + H\chi_{\text{eq}}$ from the change of variables.

The bifurcation curve is now able to be drawn in the parametric form $(A_0(\theta_{\text{eq}}), \chi_{\text{eq}}(\theta_{\text{eq}}))$. Note that the bounds imposed on θ_{eq} restrict χ_{eq} (and subsequently A_0) to physically relevant positive values.

¹This value corresponds to an experiment with vacuum permeability $\mu_0 = 4\pi \times 10^{-7} \text{ Hm}^{-1}$, rod separation $h = 0.02 \text{ m}$, spring constant $k_1 = 20 \text{ N m}^{-1}$ and magnetic dipole moments $\mathbf{m}_1 = \mathbf{m}_2 = 1 \text{ Am}^2$.

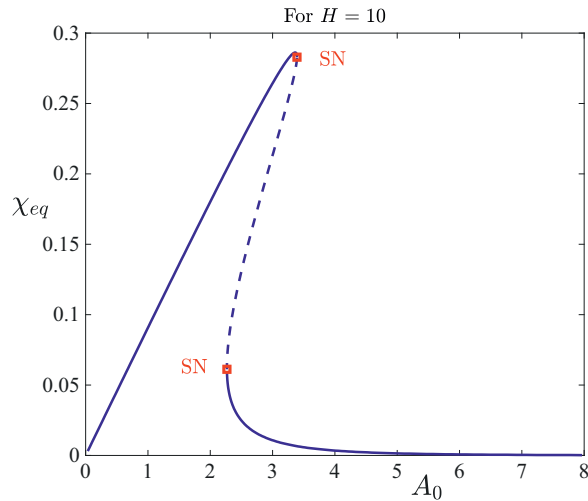


FIGURE 2. Bifurcation diagram for parameter A_0 , with $H = 10$. The two small red squares on the curve denote the locations of saddle-node bifurcations (SN) at $A_0 \approx 2.267$ and $A_0 \approx 3.392$. The dashed section indicates an unstable equilibrium.

Figure 2 displays a bifurcation diagram for the equilibrium location χ_{eq} of magnet 1, against the fixed location A_0 of magnet 2, for the illustrative case $H = 10$, and similar curves are obtained with many other values of the force H . The two small squares on the plot indicate the locations of saddle-node bifurcations, at which the curve folds over and the equilibrium location χ_{eq} for magnet 1 becomes multi-valued. For $H = 10$, these events occur at approximately $A_0 = 2.267$ and $A_0 = 3.392$.

The dashed portion of this curve signifies that the equilibrium is unstable. The stability of the equilibria in Figure 2 is obtained in the usual way, by linearization of the governing equations (3.1) near χ_{eq} . Further details are not provided here (although Section 3.3 discusses the particular case of pure centres). This then shows that, in the interval $0 \leq A_0 < 2.267$, Figure 2 indicates there is a single equilibrium and that it is a (neutrally stable) centre, characterized by pure oscillations centred about the equilibrium. At $A_0 \approx 2.267$, a second centre and a saddle are born from a saddle-node bifurcation. Then, in the interval $2.267 < A_0 < 3.392$, there are two (neutrally stable) centres separated in the phase plane by a (unstable) saddle. We shall from hereon refer to this as the bistable region in parameter space. At $A_0 \approx 3.392$, the saddle collides with the right-hand centre and both equilibria disappear in another saddle-node bifurcation, leaving the system with a single centre for $A_0 > 3.392$.

The bifurcation analysis presented above only describes the linear behaviour near the equilibria. To understand any effects of the nonlinearity in the system, phase-plane portraits are plotted for representative values of A_0 in Figures 3(a), 3(b) and 3(c) for the three values $A_0 = 1$, $A_0 = 2.5$ and $A_0 = 4$, respectively. To do this, the system (3.1) was integrated numerically from a set of initial conditions evenly spaced along

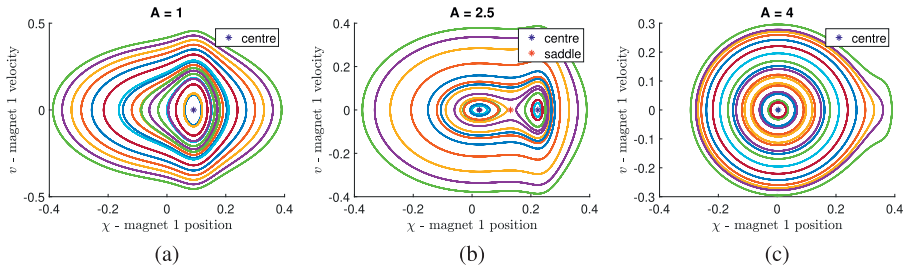


FIGURE 3. Phase portraits for $H = 10$ for the three stationary magnet 2 locations (a) $A_0 = 1$, (b) $A_0 = 2.5$ and (c) $A_0 = 4$, showing centre and saddle equilibria. Each separate curve represents a solution trajectory (with different colours).

the χ -axis, using a fourth-order Runge–Kutta method. These plots confirm that the linearized analysis does indeed give a reliable qualitative description of the true nonlinear dynamics near the equilibria. The system has two homoclinic orbits in the bi-stable region ($2.267 < A_0 < 3.392$) and a single homoclinic orbit at each saddle-node bifurcation.

The system (3.1) is an undamped ($D = 0$), autonomous, Hamiltonian system. Therefore, its solution trajectories are closed curves (here, either homoclinic or periodic) given by the level sets of the Hamiltonian (that is, by contours of constant energy). As a result, the system has a first integral, so that an algebraic expression in terms of χ and v may be found for every solution trajectory, although this is not developed further here. Further, we see from the phase portrait of the bi-stable case in Figure 3(b) that the system resembles an undamped particle in a double-well potential with two local energy minima, whereas the phase portraits shown in Figures 3(a) and 3(c) only have one local minimum at the centre.

3.2. Codimension-1 and 2 bifurcations in A and H The bifurcation diagram in Figure 2 for the single parameter $H = 10$ showed two saddle-node bifurcations, at which the curve folded to produce multiple equilibria. The parametrization technique used to produce this graph was outlined in Section 3.1 and we generalize it to track the locations of the saddle-node bifurcations for all values of H . Since these saddle-node bifurcation points occur at equilibria, the algebraic conditions in Section 3.1 still hold and a further condition must be added to them, to seek those points at which the parametrized bifurcation curve $(A_0(\theta_{eq}), \chi_{eq}(\theta_{eq}))$ becomes vertical in Figure 2. This occurs when

$$\frac{dA_0}{d\theta_{eq}} = \frac{d}{d\theta_{eq}}(\tan \theta_{eq} + H\chi_{eq}) = 0.$$

Differentiation of the parametric equations in the algorithm given in Section 3.1 yields

$$\frac{dA_0}{d\theta_{eq}} = \sec^2 \theta_{eq} + H \cos^3 \theta_{eq}(5 \cos^2 \theta_{eq} - 4) = 0.$$

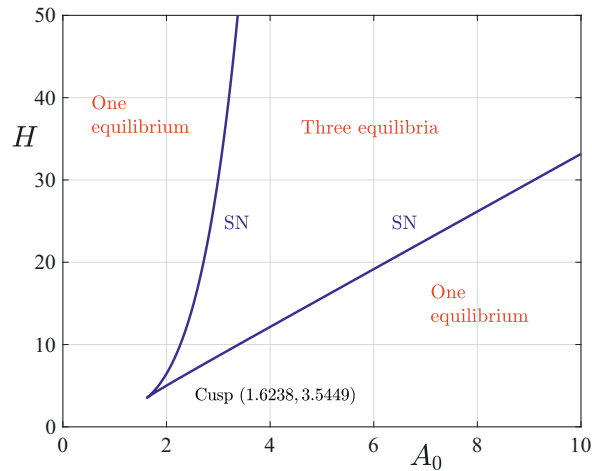


FIGURE 4. Stability diagram showing the saddle-node bifurcation curve (labelled SN) in the (A_0, H) parameter plane. At the indicated cusp point, there is a codimension-2 cusp bifurcation.

This equation is rearranged and solved for H in terms of the parameter θ_{eq} . The location of the saddle-node bifurcation, for primary bifurcation constant A_0 and unfolding constant H , is calculated from the pair of equations

$$\begin{aligned} A_0 &= \tan \theta_{\text{eq}} \left[1 + \frac{1}{(4 - 5 \cos^2 \theta_{\text{eq}})} \right], \\ H &= \frac{1}{\cos^5 \theta_{\text{eq}} (4 - 5 \cos^2 \theta_{\text{eq}})}, \end{aligned} \quad (3.3)$$

for $0 < \theta_{\text{eq}} < \pi/2$.

The saddle-node bifurcation curve is plotted in Figure 4 and was calculated in parametric form from (3.3). This diagram shows the system behaviour for all positions of magnet 2 (A_0) and force ratios (H). The bistable region (for which we have two centres and a saddle equilibrium) lies between the two saddle-node bifurcation curves, labelled SN in the diagram. A cusp forms in the saddle-node curve at approximately the point $(A_0, H) = (1.6238, 3.5449)$, and this is indicated on the figure. If $A_0 < 1.6238$, then the system is stable (with a single centre equilibrium) for all $H > 0$ and the same is true when $H < 3.5449$ as we vary A_0 .

The location of the cusp point is revealed from the parametric description of the saddle-node curve, along which the condition $dA_0/d\theta_{\text{eq}} = 0$ already applies for this codimension-1 bifurcation. To obtain the location of the cusp, which is a codimension-2 condition, we append to this the additional requirement $dH/d\theta_{\text{eq}} = 0$. This is obtained by differentiating the expression for H in the SN condition (3.3), which yields

$$\frac{dH}{d\theta_{\text{eq}}} = \frac{5 \sin \theta_{\text{eq}}(4 - 7 \cos^2 \theta_{\text{eq}})}{\cos^6 \theta_{\text{eq}}(4 - 5 \cos^2 \theta_{\text{eq}})^2} = 0.$$

The root of interest to this equation is

$$\cos^2 \theta_{\text{eq}} = 4/7,$$

and this is substituted into the parametric conditions (3.3) for the saddle-node curve. This shows that the cusp occurs at the point

$$\begin{aligned} A_0 &= 15\sqrt{3}/16 \approx 1.6238, \\ H &= 7^3\sqrt{7}/4^4 \approx 3.5449, \end{aligned}$$

and this point is indicated on the diagram in Figure 4.

3.3. Natural frequencies Here, we compute the natural frequency of each periodic orbit in the unforced and undamped system. This was done to derive a resonance condition for the forced system considered later. This will enable the forcing frequency to be related to the natural frequency of the corresponding unforced orbit.

The eigenvalues of the Jacobian matrix at a centre equilibrium give an analytic expression for the natural frequency of nearby orbits. The Jacobian matrix for our general system takes the form

$$\begin{bmatrix} 0 & 1 \\ -\mu_N^2 & -D \end{bmatrix} \quad \text{with } \mu_N^2 = 1 + \frac{H[1 - 4(A - H\chi)^2]}{[1 + (A - H\chi)^2]^{7/2}}.$$

In the absence of damping ($D = 0$), this matrix has purely imaginary eigenvalues $\pm\mu_N i$ for the centres, in which case, $\mu_N^2 > 0$. Close to a centre in the (χ, v) phase plane, the natural frequency associated with that centre at χ_{eq} is μ_N with corresponding period $2\pi/\mu_N$.

To obtain natural frequencies of orbits far from a centre in the phase plane, we return to numerical methods and take the dominant frequency from each orbit's frequency spectrum. Natural frequencies for $H = 10$ and $A = 2.4$ are illustrated in the phase plane in Figure 5(a) and along the χ -axis in Figure 5(b).

The natural frequency curve has local maxima at the centre equilibria and, as expected, approaches zero when crossing homoclinic orbits. For large displacements χ , the magnetic force becomes negligible compared with the spring force, so our natural frequency approaches that of the spring, which is 1 in our dimensionless variables.

In the forced case, to be considered later in Section 5, we will vary A between 2.4 and 2.8 for the case $H = 10$. For reference, we therefore show in Figure 6 the change in the natural frequency curve as A is varied in increments of 0.05. The movement of the sharp cusps, indicative of the homoclinic orbits, will affect the qualitative behaviour of the forced system. We use this to guide the choice of initial conditions in the subsequent section.

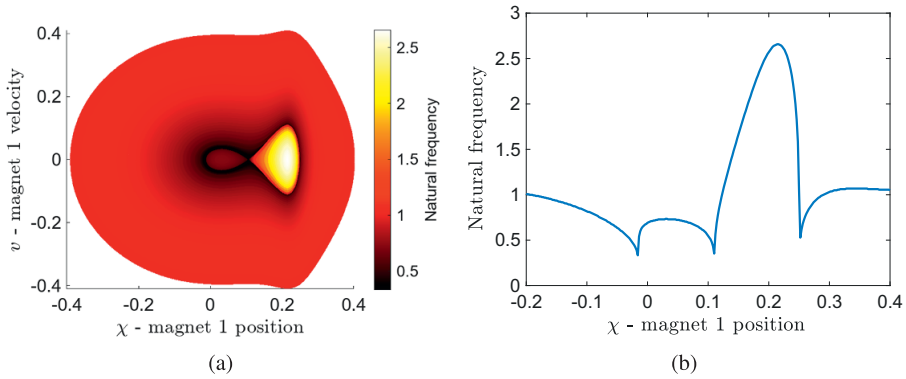


FIGURE 5. (a) Phase plane coloured by natural frequency of orbits for $H = 10$ and $A = 2.4$. (b) Natural frequencies along the χ -axis.

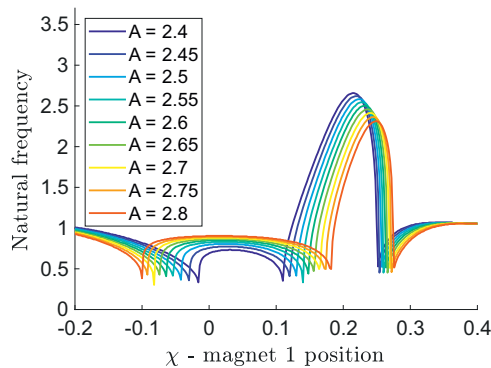


FIGURE 6. Natural frequency curves for varying A at $H = 10$.

4. Damped and forced case

4.1. Linearized forced solution The location $A(\tau)$ of the lower magnet consists of an average position A_0 plus a periodically forced component of amplitude ϵ , as described in (2.4). If ϵ is assumed to be a small parameter, then a linearized solution for the location of upper magnet 1 is obtained in the form

$$\chi(\tau) = \chi_{eq} + \epsilon X_1(\tau) + \mathcal{O}(\epsilon^2), \tag{4.1}$$

in which χ_{eq} is an equilibrium position for the magnet, calculated from (3.2). This approximate form (4.1) is substituted into the nonlinear system (2.6) and only terms of first order in ϵ are retained. This eventually leads to the linearized differential equation

$$\frac{d^2 X_1}{d\tau^2} + D \frac{dX_1}{d\tau} + (1 + H\Gamma_0)X_1 = \Gamma_0 \cos(\Omega\tau) \tag{4.2}$$

for the linearized perturbation function $X_1(\tau)$ in (4.1), where we define

$$\Gamma_0 = \frac{1 - 4(A_0 - H\chi_{\text{eq}})^2}{[1 + (A_0 - H\chi_{\text{eq}})^2]^{7/2}}. \quad (4.3)$$

The solution to the linearized equation (4.2) consists of transients, plus a periodic forced response which we write as

$$X_1(\tau) = \frac{\Gamma_0[\mathcal{T}_1 \cos(\Omega\tau) + \mathcal{T}_2 \sin(\Omega\tau)]}{(\mathcal{T}_1)^2 + (\mathcal{T}_2)^2}. \quad (4.4)$$

This expression involves the two constants

$$\mathcal{T}_1 = 1 + H\Gamma_0 - \Omega^2 \quad \text{and} \quad \mathcal{T}_2 = D\Omega.$$

For later use, we note that (4.4) describes a sinusoidal oscillation with amplitude

$$\mathcal{A}_1 = \frac{\Gamma_0}{\sqrt{(\mathcal{T}_1)^2 + (\mathcal{T}_2)^2}}. \quad (4.5)$$

In the absence of damping, $D = 0$, a (linearized) primary resonance occurs when the forcing frequency has the value

$$\Omega_{\text{res}} = \sqrt{1 + H\Gamma_0}. \quad (4.6)$$

4.2. Weakly nonlinear solution near resonance Further understanding of the *nonlinear* structure of the primary resonance in (4.4) is gained through an asymptotic analysis of the nonlinear equation (2.6) to third order, near the resonant frequency (4.6). To this end, we write

$$\begin{aligned} \chi(\tau) &= \chi_{\text{eq}} + X(\tau), \\ A(\tau) &= A_0 + A_F(\tau) \quad \text{with } A_F(\tau) = \epsilon \cos(\Omega\tau). \end{aligned}$$

To simplify the analysis, we only consider the undamped case $D = 0$ here. We further define the variable

$$Y(\tau) = A_F(\tau) - HX(\tau),$$

and carry out a Taylor-series expansion of the nonlinear equation (2.6) to third order in this variable.

After very considerable algebra, we obtain the weakly nonlinear approximate differential equation

$$\frac{d^2 Y}{d\tau^2} + (1 + H\Gamma_0)Y - H\Delta_0 Y^2 - H\Lambda_0 Y^3 = \epsilon(1 - \Omega^2) \cos(\Omega\tau).$$

In this expression, the constant Γ_0 is as defined in (4.3) and there are two additional constants

$$\Delta_0 = \frac{5Y_{\text{eq}}[3 - 4(Y_{\text{eq}})^2]}{2[1 + (Y_{\text{eq}})^2]^{9/2}},$$

$$\Lambda_0 = \frac{5[1 - 12(Y_{\text{eq}})^2 + 8(Y_{\text{eq}})^4]}{2[1 + (Y_{\text{eq}})^2]^{11/2}},$$

in which the constant $Y_{\text{eq}} = A_0 - H\chi_{\text{eq}}$ is also defined.

Near the primary resonance (4.6), we seek an approximate solution in the form

$$Y(\tau) = \mathcal{A}_W \cos(\Omega\tau) + \mathcal{B}_W \sin(\Omega\tau), \quad (4.7)$$

and retain only terms involving the forcing frequency Ω . A substantial amount of algebra gives rise to the two algebraic equations

$$\begin{aligned} \mathcal{A}_W[1 + H\Gamma_0 - \Omega^2 - \frac{3}{4}H\Lambda_0(\mathcal{A}_W^2 + \mathcal{B}_W^2)] &= \epsilon(1 - \Omega^2), \\ \mathcal{B}_W[1 + H\Gamma_0 - \Omega^2 - \frac{3}{4}H\Lambda_0(\mathcal{A}_W^2 + \mathcal{B}_W^2)] &= 0 \end{aligned} \quad (4.8)$$

for the two amplitude constants \mathcal{A}_W and \mathcal{B}_W in the assumed form (4.7) of the weakly nonlinear solution.

In the absence of damping, $D = 0$, the appropriate solution in the system (4.8) is simply $\mathcal{B}_W = 0$, from which it follows that \mathcal{A}_W satisfies the cubic equation

$$\mathcal{A}_W^3 + \frac{4[\Omega^2 - 1 - H\Gamma_0]}{3H\Lambda_0}\mathcal{A}_W + \frac{4\epsilon(1 - \Omega^2)}{3H\Lambda_0} = 0. \quad (4.9)$$

Since this cubic has either one or three real roots for \mathcal{A}_W , it follows from (4.9) that, near the primary resonance, there is either one or else three forced orbits, and this is discussed more fully in Section 5.6. To solve this equation numerically for a given Ω , we cast (4.9) in terms of a companion matrix and then used MATLAB's `eig` routine to calculate the roots \mathcal{A}_W , keeping only those with zero imaginary part.

4.3. Computing forced periodic orbits As a check on the weakly nonlinear results of Section 4.2, we also compute periodic forced oscillations of the fully nonlinear model (2.4). We express the displacement of the upper mass in the form

$$\chi(\tau) = C_0 + \sum_{n=1}^N [C_n \cos(n\Omega\tau) + S_n \sin(n\Omega\tau)], \quad (4.10)$$

and use Newton's method to calculate the vector of coefficients

$$\mathbf{u} = [C_0, C_1, \dots, C_N; S_1, \dots, S_N].$$

The number N of Fourier modes in (4.10) is taken to be as large as practicable and we use $N = 151$. The Newton–Galerkin method we employ involves multiplying the nonlinear ODE (2.6) successively by the basis functions $\cos(\ell\Omega\tau)$, $\ell = 0, 1, 2, \dots, N$

and $\sin(\ell\Omega\tau)$, $\ell = 1, 2, \dots, N$, and integrating over one period $0 < \tau < 2\pi/\Omega$. This creates the error vector

$$\mathbf{E} = [E_0, E_1, \dots, E_N; E_{N+1}, \dots, E_{2N+1}].$$

This has components

$$\begin{aligned} E_0 &= C_0 - \frac{\Omega}{2\pi} \mathcal{R}_0^{(C)}, \\ E_\ell &= C_\ell [1 - \ell^2 \Omega^2] + S_\ell (D\ell\Omega) - \frac{\Omega}{\pi} \mathcal{R}_\ell^{(C)}, \quad \ell = 1, \dots, N, \\ E_{N+\ell} &= -C_\ell (D\ell\Omega) + S_\ell [1 - \ell^2 \Omega^2] - \frac{\Omega}{\pi} \mathcal{R}_\ell^{(S)}, \quad \ell = 1, \dots, N, \end{aligned}$$

in which we define

$$\begin{aligned} \mathcal{R}_\ell^{(C)} &= \int_0^{2\pi/\Omega} \frac{[A(\tau) - H\chi] \cos(\ell\Omega\tau)}{(1 + [A(\tau) - H\chi]^2)^{5/2}} d\tau, \quad \ell = 0, 1, 2, \dots, N, \\ \mathcal{R}_\ell^{(S)} &= \int_0^{2\pi/\Omega} \frac{[A(\tau) - H\chi] \sin(\ell\Omega\tau)}{(1 + [A(\tau) - H\chi]^2)^{5/2}} d\tau, \quad \ell = 1, 2, \dots, N. \end{aligned}$$

Newton’s method is used to solve the system of algebraic equations $\mathbf{E}(\mathbf{u}) = \mathbf{0}$. This creates the coefficients needed in the Fourier representation (4.10) of the displacement $\chi(\tau)$. The amplitude of these nonlinear periodic solutions calculated from the numerical solution is then

$$\mathcal{A}_N = \frac{1}{2}(\max\{\chi(\tau)\} - \min\{\chi(\tau)\}). \tag{4.11}$$

5. Parametrically forced case

The location $A(\tau)$ of magnet 2 will now be varied sinusoidally, according to the function (2.4) introduced in Section 2. The dimensionless forcing frequency is Ω , and magnet 2 is driven sinusoidally between locations A_1 and A_2 . We again choose $H = 10$, and will drive magnet 2 sinusoidally so that it oscillates between locations $A_1 = 2.4$ and $A_2 = 2.8$. It follows from (2.5) that the mean location of magnet 2 is therefore $A_0 = 2.6$ and the forcing amplitude is $\epsilon = 0.2$. From Figure 4, this parameter regime is chosen to coincide with the values of A over which the corresponding unforced system would be in its bistable region. This is done with the aim of observing the most interesting and exotic dynamics of which the system is capable, since, when three equilibria are present in the unforced case, we expect that forcing may result in solution trajectories intermittently “jumping” between potential wells. As $A(\tau)$ varies with time, the corresponding three equilibria for magnet 1 in the unforced case effectively oscillate along the χ -axis, from the three locations $\chi_{\text{eq}} = (0.0316, 0.1106, 0.215)$ for $A_1 = 2.4$ to the three positions $\chi_{\text{eq}} = (0.0144, 0.1819, 0.2485)$ for $A_2 = 2.8$.

For each forcing frequency Ω investigated, solution trajectories were observed to exhibit one of four general behaviour types, depending on initial conditions; these are

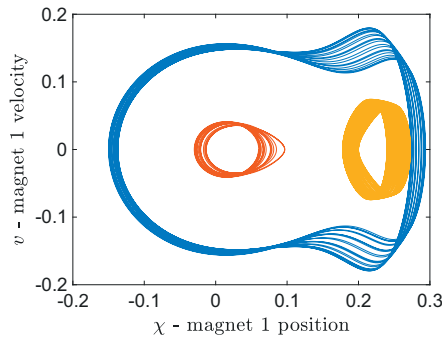


FIGURE 7. Examples of quasiperiodic orbits for $\Omega = 0.1$. The initial conditions used were $v_0 = 0$ and $\chi_0 = -0.15$ for the large orbit (Γ_b in blue), $\chi_0 = 0.06$ for the left-hand smaller orbit (Γ_r in red) and $\chi_0 = 0.2$ for the smaller right-hand orbit (Γ_y in yellow).

quasiperiodic, chaotic, periodic or resonant solutions. Characteristic examples for each behaviour type are presented.

5.1. Solution behaviour: quasiperiodic orbits We first explore quasiperiodic orbits, which appear in areas of phase space sufficiently far from the homoclinic connections of the unforced system. Example trajectories of this type in phase space for $\Omega = 0.1$ are shown in Figure 7. Because this is a *forced* system, solution trajectories are now objects in a higher-dimensional phase space and so cannot be characterized purely using the (χ, v) phase *plane* as for the previous Section 3. Nevertheless, the quasiperiodic orbits in Figure 7 are presented here as projections onto the χ, v axes, which contain some memory of the unforced system. Thus, there is a moderate-amplitude quasiperiodic orbit centred on the left-hand unforced equilibrium (drawn in red) and a second one centred on the right-hand equilibrium (drawn in yellow). We denote these orbits as Γ_r and Γ_y , respectively. A quasiperiodic orbit of much larger amplitude (in blue) surrounds all three equilibria. This is denoted as Γ_b . These three solution trajectories were obtained simply by varying the initial value of χ , so that $\chi_0 = 0.06, 0.2$ and -0.15 . The initial condition of v was set as $v_0 = 0$ for all three.

To explore further the indicators of quasiperiodicity, we focus on Γ_r in Figure 7 (obtained with $\chi_0 = 0.06$). Its time series $\chi(\tau)$ is drawn in Figure 8(a) and shows the almost-periodic nature of the orbit. We also plot the frequency spectrum of its time series in Figure 8(b). This was generated via a discrete Fourier transform of the time-series data. For a quasiperiodic orbit, we expect the solution to consist of a finite number of distinct frequencies which, importantly, are not all rational multiples of each other. This is not immediately discernible from the frequency spectrum so we turn to additional indicators of quasiperiodicity.

We construct a stroboscopic map for the example orbit by sampling our trajectory (starting at time $\tau = 0$) with a “stroboscopic period” equal to our parametric forcing period;

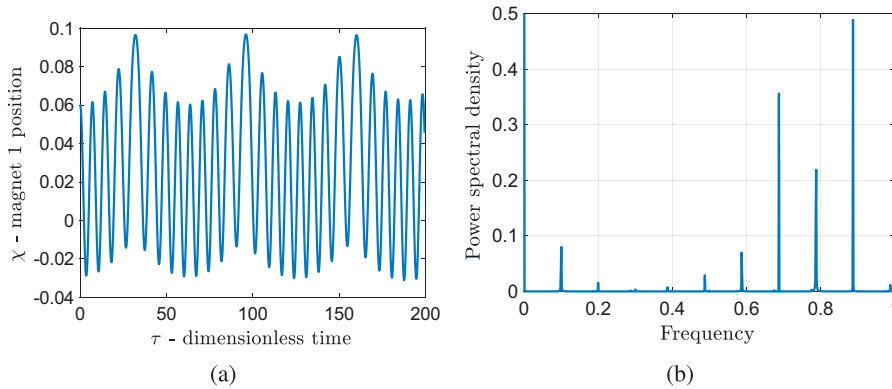


FIGURE 8. (a) Example time series $\chi(\tau)$ for Γ_r in Figure 7 and (b) the corresponding frequency spectrum showing a discrete set of frequencies.

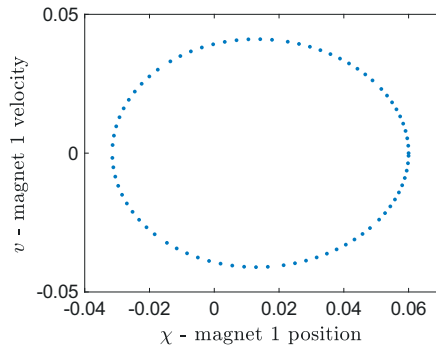


FIGURE 9. Stroboscope map for Γ_r in Figure 7, showing densely spaced points on a closed loop.

that is, we let $T_{\text{strobe}} = 2\pi/\Omega$. For quasiperiodic orbits, the stroboscopic map shows a set of densely spaced points on a closed loop. This is illustrated in Figure 9.

If we display the position of magnet 2 $A(\tau)$ as a third dimension of our system, then quasiperiodic trajectories $(\chi(\tau), v(\tau), A(\tau))$ lie on the surface of an “invariant” torus for all time τ ¹. Figure 10 illustrates this torus for Γ_r from Figure 7, which was obtained with initial condition $\chi_0 = 0.06$.

5.2. Solution behaviour: chaotic orbits A second type of behaviour occurs in these forced orbits when a trajectory jumps between quasiperiodic orbits that enclose one or both centres. An illustration of such behaviour for this system is given in Figure 11. This diagram is again produced with forcing frequency $\Omega = 0.1$. The solution was started from rest ($v_0 = 0$), with initial displacement $\chi_0 = -0.08$ for magnet 1. In terms of the earlier analogy in which the unforced system was likened to

¹Due to the periodic nature of the parameter $A(\tau)$, the stroboscope map is actually a Poincaré cross-section through the torus at $A = A(0) = 2.8$ in the case considered here.

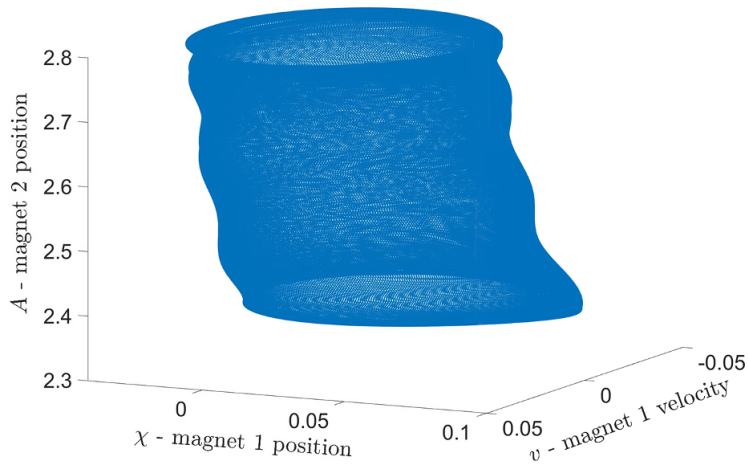


FIGURE 10. Invariant torus for Γ_r ($\chi_0 = 0.06$) shown in Figure 7.

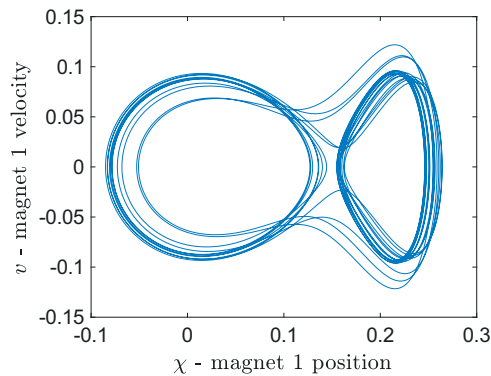


FIGURE 11. Example of chaotic orbit for $\Omega = 0.1, \chi_0 = -0.08, v_0 = 0$.

a particle in a double well, the forced particle here can be thought of as transitioning between small oscillations in either well and large oscillations covering both wells when it gains enough energy. Such jumps occur intermittently – without a fixed period – so the solution is genuinely chaotic. These intermittent jumps may be seen more clearly from the time series for the trajectory, which is presented in Figure 12(a). The frequency spectrum for this solution shows a *continuous* distribution of frequencies, as is expected for chaos. This is illustrated in Figure 12(b).

We also computed Lyapunov exponents for this orbit, using the QR decomposition method [3] with 250 000 samples from $\tau = 0$ to $\tau = 5000$. This resulted in $\lambda_1 = 0.0239$ and $\lambda_2 = -0.0239$. As λ_1 is a nonnegligible positive value, this implies that nearby trajectories diverge exponentially, thus providing further evidence that the solution presented in Figure 11 is indeed chaotic.

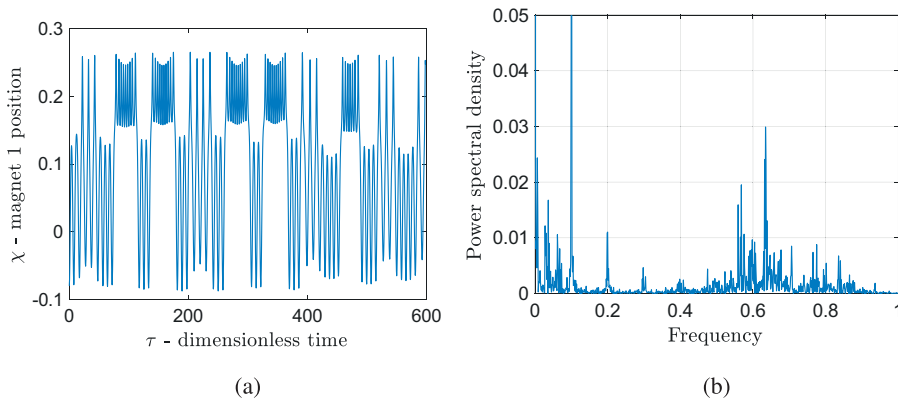


FIGURE 12. (a) Example time series $\chi(\tau)$ of chaotic orbit with $\Omega = 0.1$, $\chi_0 = -0.08$, $v_0 = 0$ showing intermittent jumps. (b) The corresponding frequency spectrum showing a continuous set of frequencies.

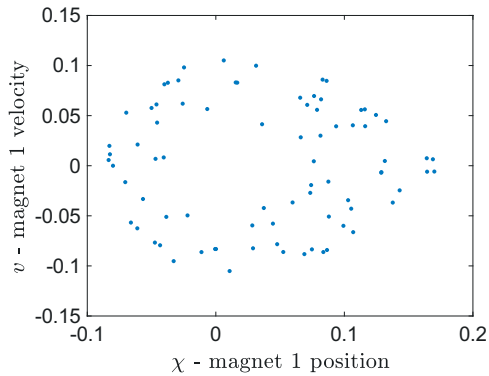


FIGURE 13. Stroboscope map for the chaotic orbit filling out a 2D region of the (χ, v) plane at $A = 2.8$.

With the forcing function A represented as an extra dimension, the chaotic trajectory $(\chi(\tau), v(\tau), A(\tau))$ illustrated above now lies within the volume of a strange attractor in the phase space. Iterates of the corresponding stroboscopic map now fill out a 2D region in the (χ, v) -plane, displayed in Figure 13¹.

5.3. Solution behaviour: periodic orbits A third type of behaviour in this forced system consists of periodic orbits, which enclose either a single centre or jump between them in a fixed pattern. Three such periodic orbits are shown in Figure 14. There are two small orbits centred on the left and right equilibria of the unforced system, and a third large orbit that encloses all three of the equilibria.

¹Again, this stroboscopic map is the Poincaré cross-section of the strange attractor on the plane $A = 2.8$ in the phase space.

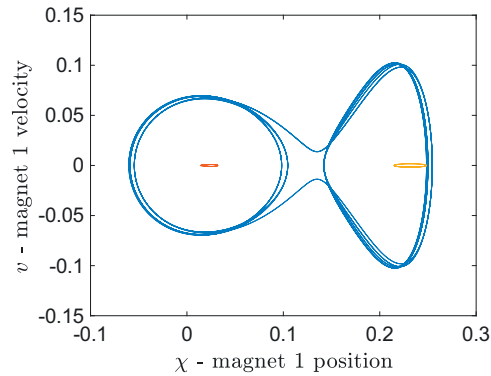


FIGURE 14. Three periodic orbits for the forced system with $\Omega = 0.1$. The initial conditions used were $v_0 = 0$ and $\chi_0 = -0.0603, 0.0144, 0.2486$ for the large orbit (in blue), smaller left orbit (in red) and the smaller right orbit (in yellow), respectively.

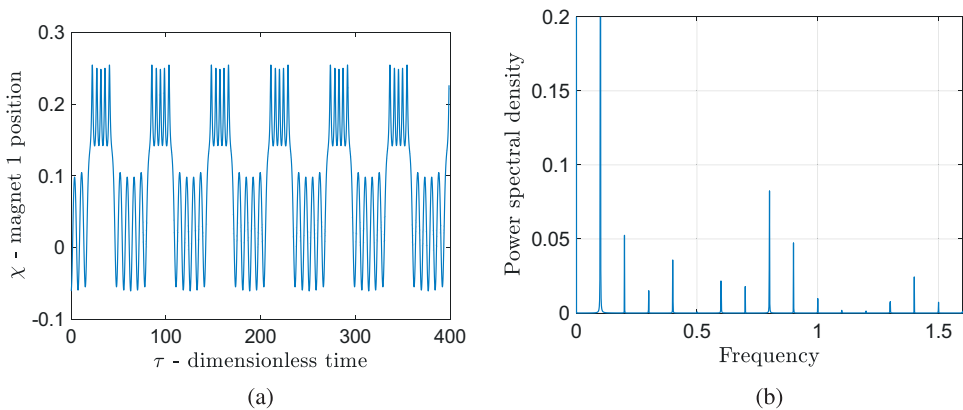


FIGURE 15. (a) Example time series $\chi(\tau)$ of periodic orbit with $\Omega = 0.1, \chi_0 = -0.0603, v_0 = 0$ showing regular jumps between centres. (b) The corresponding frequency spectrum contains only integer multiples of $\Omega = 0.1$.

It is instructive to consider the large-amplitude forced periodic orbit (in blue) in Figure 14 in greater detail. This solution was generated from initial condition $\chi_0 = -0.0603$. The time series $\chi(\tau)$ for this solution is shown in Figure 15(a), and clearly illustrates the periodic jumps between orbits centred around the left and right centre equilibria of the unforced system. The periodic nature of this solution is underscored by its frequency spectrum presented in Figure 15(b), since this consists of spikes only at integer multiples of the driving frequency (which is also the frequency of the orbit). This is further supported by the stroboscopic map, which contains only a single point and is not shown here in the interest of space.

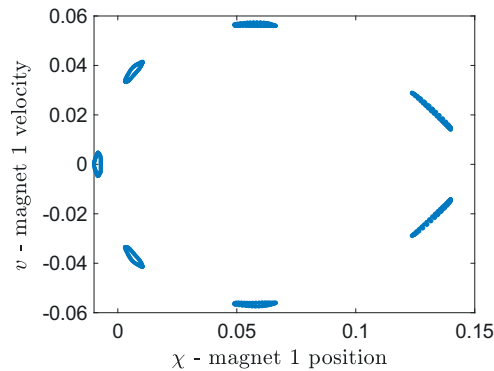


FIGURE 16. Stroboscope map for an $s = 7$ resonant orbit obtained with $\Omega = 0.9, \chi_0 = -0.01, v_0 = 0$, showing a chain of 7 KAM islands.

5.4. Solution behaviour: resonant orbits A fourth behaviour type is a resonant quasiperiodic or periodic orbit. The quasiperiodic case presents itself on the stroboscope map as a number of disjoint closed loops and an example of these is presented in Figure 16, obtained for frequency $\Omega = 0.9$ and with initial conditions $\chi_0 = -0.01, v_0 = 0$. These structures are a consequence of the Kolmogorov–Arnol’d–Moser theory in resonant Hamiltonian systems (see [5, pages 219–223]) and are referred to as “KAM island chains” in some modern literature such as that by Kroetz et al. [9] and Nieto et al. [13]. A chain of s islands implies the existence of a resonant periodic orbit with frequency Ω/s that traverses the island centres (centres of closed loops in Figure 16) in a given order. The corresponding trajectory for this $s = 7$ quasiperiodic resonant orbit is illustrated in Figure 17. We find that stroboscope maps, such as in Figure 16, are most convenient for identifying resonances, because the phase plane trajectory (Figure 17), the frequency spectrum and the Lyapunov exponents (here, $\lambda_\chi = 0.00093, \lambda_v = -0.00093$); otherwise, all appear similar to those of a nonresonant orbit.

We again extend the phase space by including as an additional axis the forcing function $A(\tau)$. This creates an invariant torus for the $s = 7$ resonant solution and the resulting structure is plotted in Figure 18. This gives a long and twisted object in the phase space, compared with a nonresonant quasiperiodic orbit, and the structure in Figure 18 intersects the $A = 2.8$ plane $s = 7$ times.

5.5. Damped solution behaviour When a sufficiently small amount of damping is introduced ($D < 10^{-3}$), periodic and resonant periodic forced orbits of the undamped system are preserved. Damping causes nearby trajectories to be drawn towards them. To illustrate this, we return to the $s = 7$ resonance from Section 5.4. We sample initial conditions within the leftmost KAM island in Figure 16 (for which $-0.01 < \chi < -0.007$) and apply damping $D = 0.0005$. The resulting layered stroboscope map is shown in Figure 19. Trajectories that start from initial conditions that are sufficiently close to the island centre (periodic resonance) are drawn towards the resonance as a

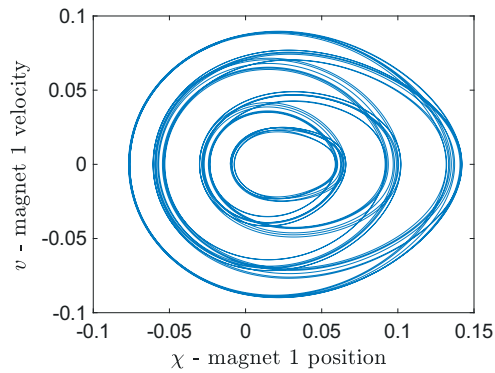


FIGURE 17. Example of the trajectory for the $s = 7$ resonant orbit obtained with $\Omega = 0.9, \chi_0 = -0.01, v_0 = 0$.

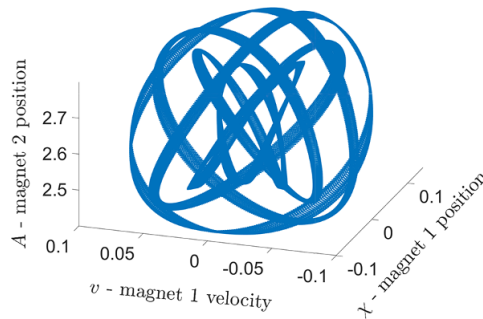


FIGURE 18. Invariant torus for the $s = 7$ resonant orbit.

result of the damping, while others move towards a different nonresonant periodic orbit. As damping is increased to $D = 0.001$, the $s = 7$ resonance is destroyed and initial conditions in Figure 19 lead to trajectories that are all damped towards the nonresonant periodic orbit.

5.6. Observed behaviours for varying driving frequency Ω We now explore the possible system behaviours for a range of parametric driving frequencies Ω . We return briefly to a discussion of the solution near primary resonance, examined in Section 4. For definiteness, we again consider separation distance $H = 10$ and average location $A_0 = 2.6$ of the lower forcing magnet, illustrated in Figures 2–6. Figure 4 shows that the unforced system (3.1) possesses three different equilibria χ_{eq} at these parameter values; when subject to forcing, each of these equilibria develops its own complicated resonance structure, resulting in solution behaviour of extraordinary complexity at certain forcing frequencies Ω .

For brevity, we consider only the forced periodic behaviour of the lowest of these three equilibria at $H = 10$ and $A_0 = 2.6$, for which $\chi_{\text{eq}} = 0.020275$ (see Figure 2). This

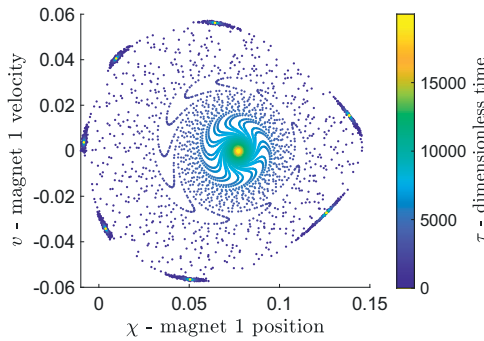


FIGURE 19. Layered stroboscope maps of initial conditions close to the $s = 7$ resonance with damping. Initial conditions sufficiently close to the island centre are damped towards the resonance, but others are damped towards some nonresonant periodic orbit. Colour indicates the time along each trajectory.

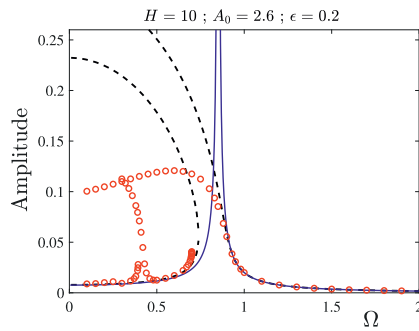


FIGURE 20. The response amplitudes for three different approximations near the primary resonance of the lowest equilibrium point, with $H = 10$, $A_0 = 2.6$ and forcing amplitude $\epsilon = 0.2$. The solid blue line represents the linearized forced solution amplitude $\epsilon \mathcal{A}_1$, the dashed black lines are the predictions of the weakly nonlinear amplitude \mathcal{A}_W and the red circles are fully nonlinear amplitudes \mathcal{A}_N .

is subject to forcing with amplitude $\epsilon = 0.2$ and over a variety of driving frequencies Ω , and the results are illustrated in Figure 20. The solid blue lines correspond to values of the linearized forcing amplitude $\epsilon \mathcal{A}_1$ calculated from (4.5) in Section 4.1. There is a primary (linearized) resonance at the frequency $\Omega_{\text{res}} \approx 0.8511$ given in (4.6) at which the linearized amplitude $\epsilon \mathcal{A}_1$ is predicted to increase without bound. The predictions of the weakly nonlinear solution of Section 4.2 are also shown in Figure 20 and are drawn using dashed black lines. These are the weakly nonlinear amplitudes \mathcal{A}_W obtained from the cubic equation (4.9), and they show that nonlinear effects are responsible for bending the resonance peak to the left of the diagram, to produce three simultaneous periodic forced solutions for frequencies Ω below that of the primary resonance. This prediction is confirmed, at least qualitatively, by the numerical periodic solution of Section 4.3, for which the nonlinear solution amplitudes \mathcal{A}_N at different frequencies Ω were computed using (4.11). These are shown

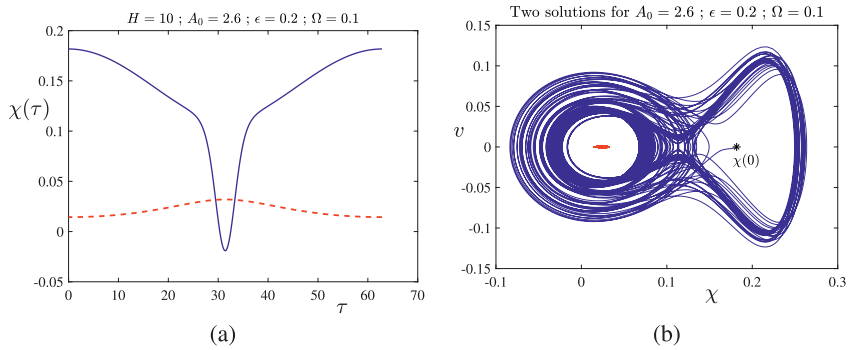


FIGURE 21. (a) Two solutions computed by integrating forward in time from the two periodic solutions at $\Omega = 0.1$ taken from Figure 20 ($0 < \tau < 2000$). (b) The smaller-amplitude solution (red line) remains periodic, but the large-amplitude solution (solid blue lines) is drawn into a chaotic strange attractor.

by small red circles. Two distinct forced nonlinear solutions are computed numerically, and while a third is suspected, it was not able to be obtained. In addition, the nonlinear results also show the emergence of the first superharmonic resonance at approximately $\Omega = 0.4$ and this is evident in Figure 20.

The resonance structure shown in Figure 20 pertains only to the lowest of three equilibria possible at the parameter values $H = 10$, $A_0 = 2.6$. Additional resonances are possible from the other two equilibria, so that many more periodic forced orbits than shown in Figure 20 are expected. In addition, quasi-periodic and chaotic solutions are also possible, so that the nonlinear solutions in Figure 20 are likely to be embedded in an extremely complex solution environment. Their stability is therefore of interest.

We first illustrate two different nonlinear periodic solutions at the forcing frequency $\Omega = 0.1$ in Figure 21(a). These two solutions correspond to the two red circles at the left-most value of Ω in Figure 20 and were obtained using the algorithm described in Section 4.3. These show the displacement χ as a function of time τ over a single period $0 < \tau < 2\pi/\Omega$. The smaller-amplitude solution sketched with red dashed lines is the lower of the two points in Figure 20 and is approximated very closely by the linearized solution (4.4). The larger solution in Figure 21(a), sketched using a solid blue line, comes from the upper branch of the primary resonance in Figure 20 and its behaviour with time is clearly highly nonsinusoidal.

The stability of the two solutions shown in Figure 21(a) has been examined here simply by integrating the nonlinear equations (2.6) forward in time for $0 < \tau < 2000$, starting with initial values taken from these two periodic forced solutions at $\Omega = 0.1$. The results are shown as trajectories in the (χ, v) -plane in Figure 21(b). The smaller-amplitude solution remains periodic in time and so it appears simply as a small-amplitude ellipse in Figure 21(b) (in red). This small-amplitude periodic solution is therefore stable. By contrast, the large-amplitude solution is rapidly drawn away from the periodic configuration in Figure 21(a) and onto the strange attractor of

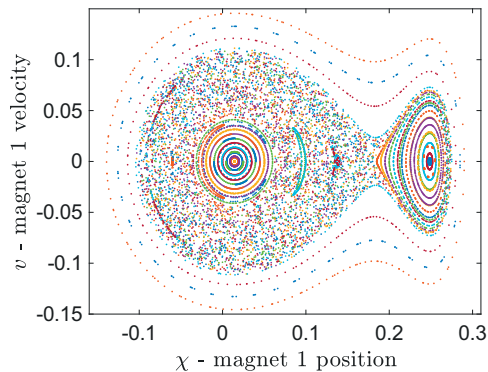


FIGURE 22. Layered stroboscope maps for $\Omega = 0.1$.

a genuinely chaotic orbit. This is also shown in Figure 21(b) (in blue), where the initial point $\chi(0)$ is sketched with an asterisk, after which the trajectory produces the chaotic orbit indicated.

The forced periodic orbits in Figures 20–21(b) exist within a highly complex solution environment and so we conclude this presentation of results by examining how this changes with increasing forcing frequency Ω . This is done by layering stroboscope maps computed for a large sample of initial conditions (taken along the χ -axis and with $A(0) = 2.8$). The resulting maps give an overview of which initial conditions lead to which behaviour type. Areas densely filled with points are regions of chaos, corresponding to a slice through the strange attractor in the (χ, v, A) phase space. Single closed loops correspond to quasiperiodic orbits (QPOs), while multiple disjoint closed loops correspond to resonant orbits. Notice that, since QPOs and resonances only fill out curves and not areas in the (χ, v) -plane, we will often fail to observe such orbits with our sample of initial conditions. Hence, it is likely that any empty “holes” in the chaotic region may contain such orbits. We also note that some loops corresponding to a QPO may not appear closed (that is, they may have a “dashed” appearance), but this is simply an artefact of insufficient integration time. The evolution of the strange attractor slice as Ω increases is explored in Figures 22–25.

The layered stroboscope map for $\Omega = 0.1$, shown in Figure 22, indicates a chaotic region containing two large holes. These are regions corresponding to QPOs and resonant orbits. The outer region surrounding the attractor also contains QPOs and resonant orbits, but these are not easily seen in Figure 22 due to the small sample of initial conditions. In Figure 23, the forcing frequency is increased to the value $\Omega = 0.9$ and, as a result, the chaotic attractor region changes shape. In particular, the holes in its structure are reduced in size.

In Figure 24, the forcing frequency is increased to the value $\Omega = 1$. Surprisingly, for this case, chaotic trajectories are not observed in the small region of the (χ, v) solution space illustrated (although they do occur at much larger amplitudes). Consequently,

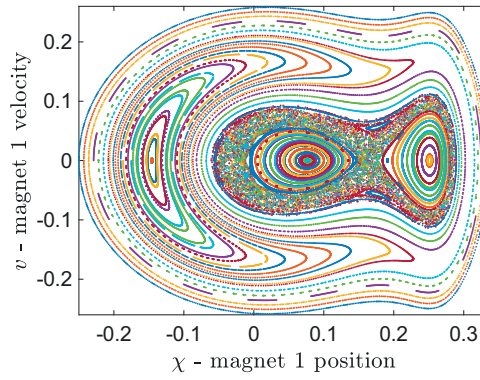


FIGURE 23. Layered stroboscope maps for $\Omega = 0.9$.

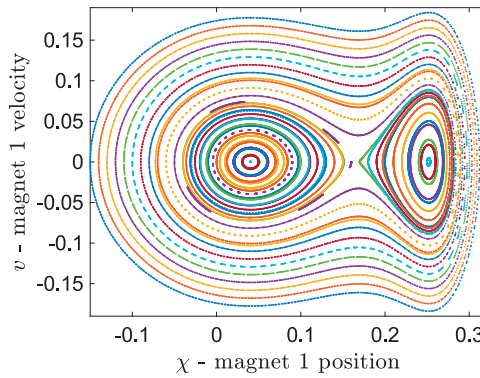


FIGURE 24. Layered stroboscope maps for $\Omega = 1$, showing only quasi-periodic orbits.

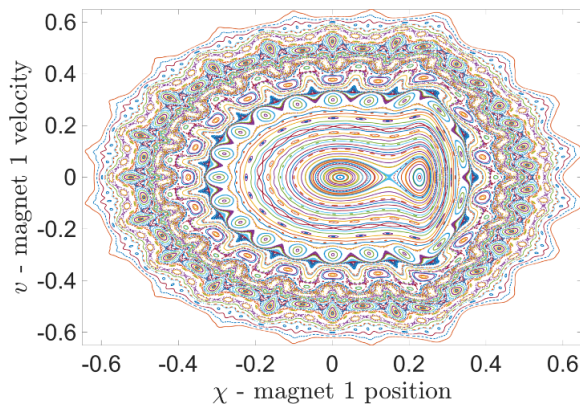


FIGURE 25. Layered stroboscope maps for $\Omega = 20$.

the trajectories shown consist of QPOs only and there even do not appear to be any resonant orbits.

For $\Omega = 20$ (the highest frequency tested), the attractor appears to break apart into multiple “bands” of chaos, separated by regions of QPOs and resonant orbits. This results in the beautiful and elaborate layered stroboscopic map shown in Figure 25.

6. Discussion

This paper presents a comprehensive dynamical analysis of a magneto-mechanical oscillator that displays a rich set of nonlinear behaviour types, despite its deceptive apparent simplicity. The study first looked at the unforced and undamped (Hamiltonian) case, which resembled an oscillator with a double-well potential. Solutions consist of families of periodic orbits and in some cases, homoclinic connections. A two-parameter bifurcation diagram in the force ratio H and magnet 2 position A_0 revealed a cusp bifurcation and corresponding bistable region in parameter space. Natural frequencies of periodic orbits were plotted for a cross-section of initial conditions and over the interval of values of A that would later be encountered in the parametrically forced case. These frequency curves were used to inform the choice of initial conditions when parametrically forcing the system. This was done additionally with the aim of deriving a resonance condition, although this was not successful in any case other than the primary resonance condition ($\Omega = 1$) and so remains as an area of further research.

Parametrically forcing the system, by sinusoidally varying the location $A(\tau)$ of magnet 2 with frequency Ω in the bistable parameter region, generated a mixture of quasiperiodic, periodic and chaotic solutions, in addition to higher-order (quasiperiodic/periodic) resonances. Solution types are discussed and characterized using phase-plane plots, time series, power spectra, stroboscopic maps and Lyapunov exponents. Stroboscope maps are found to be particularly useful in identifying resonances, which present as chains of KAM islands. To investigate which solution types are present for different driving frequencies Ω , stroboscope maps were computed for a large number of initial conditions and layered (that is, plotted on the same axes) to reveal regions of integrable and chaotic dynamics in the phase plane. It was found that the chaotic attractor grows and breaks apart as Ω increases, and is briefly destroyed when the system is driven at precisely the natural frequency of the spring–mass system. Adding sufficiently weak damping to the system resulted in trajectories being damped towards nearby periodic orbits or resonances. Resonances were destroyed when damping was strong enough, leaving trajectories to be damped towards nonresonant periodic orbits.

Acknowledgement

We would like to thank two anonymous reviewers for their valuable insight and suggestions which greatly improved our manuscript.

References

- [1] L.-Q. Chen and Y. Fan, “Internal resonance vibration-based energy harvesting”, *Nonlinear Dyn.* **111** (2023) 11703–11727; doi:[10.1007/s11071-023-08464-0](https://doi.org/10.1007/s11071-023-08464-0).
- [2] J. M. Christian and H. A. J. Middleton-Spencer, *Chaos in the magnetic pendulum* (April 2020). <https://ima.org.uk/13908/chaos-in-the-magnetic-pendulum/>.
- [3] L. Dieci, R. D. Russell and E. S. Van Vleck, “On the computation of Lyapunov exponents for continuous dynamical systems”, *SIAM J. Numer. Anal.* **34** (1997) 402–423; doi:[10.1137/S0036142993247311](https://doi.org/10.1137/S0036142993247311).
- [4] L. K. Forbes, “Forced transverse oscillations in a simple spring–mass system”, *SIAM J. Appl. Math.* **51** (1991) 1380–1396; doi:[10.1137/0151069](https://doi.org/10.1137/0151069).
- [5] J. Guckenheimer and P. Holmes, *Nonlinear oscillations, dynamical systems, and bifurcations of vector fields* (Springer-Verlag, New York, 1983).
- [6] Z. Hao, D. Wang and M. Wiercigroch, “Nonlinear dynamics of new magneto-mechanical oscillator”, *Commun. Nonlinear Sci. Numer. Simul.* **105** (2022) Article ID: 106092; doi:[10.1016/j.cnsns.2021.106](https://doi.org/10.1016/j.cnsns.2021.106).
- [7] R. A. Ibrahim, “Recent advances in nonlinear passive vibration isolators”, *J. Sound Vib.* **314** (2008) 371–452; doi:[10.1016/j.jsv.2008.01.014](https://doi.org/10.1016/j.jsv.2008.01.014).
- [8] R. Kandasamy, F. Cui, N. Townsend, C.-C. Foo, J. Guo, A. Shenoj and Y. Xiong, “A review of vibration control methods for marine offshore structures”, *Ocean Eng.* **127** (2016) 279–297; doi:[10.1016/j.oceaneng.2016.10.001](https://doi.org/10.1016/j.oceaneng.2016.10.001).
- [9] T. Kroetz, J. S. E. Portela and R. L. Viana, “Coexistence of subharmonic resonant modes obeying a period-adding rule”, *Int. J. Bifurcation Chaos* **28** (2018) Article ID: 1830031; doi:[10.1142/S0218127418300318](https://doi.org/10.1142/S0218127418300318).
- [10] K. A. Kumar, S. F. Ali and A. Arockiarajan, “Magneto-elastic oscillator: modeling and analysis with nonlinear magnetic interaction”, *J. Sound Vib.* **393** (2017) 265–284; doi:[10.1016/j.jsv.2017.01.007](https://doi.org/10.1016/j.jsv.2017.01.007).
- [11] B. P. Mann and B. A. Owens, “Investigations of a nonlinear energy harvester with a bistable potential well”, *J. Sound Vib.* **329** (2010) 1215–1226; doi:[10.1016/j.jsv.2009.11.034](https://doi.org/10.1016/j.jsv.2009.11.034).
- [12] F. C. Moon and P. J. Holmes, “A magnetoelastic strange attractor”, *J. Sound Vib.* **65** (1979) 275–296; doi:[10.1016/0022-460X\(79\)90520-0](https://doi.org/10.1016/0022-460X(79)90520-0).
- [13] A. R. Nieto, J. M. Seoane, R. Barrio and M. A. F. Sanjuán, “A mechanism explaining the metamorphoses of KAM islands in nonhyperbolic chaotic scattering”, *Nonlinear Dyn.* **109** (2022) 1123–1133; doi:[10.1007/s11071-022-07623-z](https://doi.org/10.1007/s11071-022-07623-z).
- [14] R. K. Pal, M. Ruzzene and J. J. Rimoli, “A continuum model for nonlinear lattices under large deformations”, *Int. J. Solids Structures* **96** (2016) 300–319; doi:[10.1016/j.ijsolstr.2016.05.020](https://doi.org/10.1016/j.ijsolstr.2016.05.020).
- [15] H. Sarafian, “Dynamic dipole-dipole magnetic interaction and damped nonlinear oscillations”, *J. Electromagn. Anal. Appl.* **1** (2009) 195–204; doi:[10.4236/jemaa.2009.14030](https://doi.org/10.4236/jemaa.2009.14030).
- [16] B. Yan, N. Yu and C. Wu, “A state-of-the-art review on low-frequency nonlinear vibration isolation with electromagnetic mechanisms”, *Appl. Math. Mech. (English Ed.)* **43** (2022) 1045–1062; doi:[10.1007/s10483-022-2868-5](https://doi.org/10.1007/s10483-022-2868-5).
- [17] Z. Yang, S. Zhou, J. Zu and D. Inman, “High-performance piezoelectric energy harvesters and their applications”, *Joule* **2** (2018) 642–697; doi:[10.1016/j.joule.2018.03.011](https://doi.org/10.1016/j.joule.2018.03.011).
- [18] K. W. Yung, P. B. Landecker and D. D. Villani, “An analytic solution for the force between two magnetic dipoles”, *Magn. Elect. Separat.* **9** (1998) 39–52; doi:[10.1155/1998/79537](https://doi.org/10.1155/1998/79537).